Multidimensional Tensor-Based Inductive Thermography With Multiple Physical Fields for Offshore Wind Turbine Gear Inspection

Bin Gao, *Senior Member, IEEE*, Yunze He, *Member, IEEE*, Wai Lok Woo, *Senior Member, IEEE*, Gui Yun Tian, *Senior Member, IEEE*, Jia Liu, and Yihua Hu, *Senior Member, IEEE*

Abstract—Condition monitoring (CM), fault diagnosis (FD), and nondestructive testing (NDT) are currently considered crucial means to increase the reliability and availability of wind turbines. Many research works have focused on CM and FD for different components of wind turbine. Gear is typically used in a wind turbine. There is insufficient space to locate the sensors for long-term monitoring of fatigue state of gear, thus, offline inspection using NDT in both manufacturing and maintenance processes are critically important. This paper proposes an inductive thermography method for gear inspection. The ability to track the properties variation in gear such as electrical conductivity, magnetic permeability, and thermal conductivity has promising potential for the evaluation of material state undertaken by contact fatigue. Conventional thermography characterization methods are built based on single physical field analysis such as heat conduction or in-plane eddy current field. This study develops a physics-based multidimensional spatial-transient-stage tensor model to describe the thermo optical flow pattern for evaluating the contact fatigue damage. A helical gear with different cycles of contact fatigue tests was investigated and the proposed method was verified. It indicates that the proposed methods are effective tool for gear inspection and fatigue evaluation, which is important for early warning and condition-based maintenance.

Index Terms—Fatigue, gears, imaging inspection, inductive thermography, multidimensional tensor model, thermo optical flow.

NOMENCLATURE

A capital boldfaced letter is used to denote a matrix. A small boldfaced letter denotes a column vector, unless specified otherwise. Some notational symbols are listed below.

$\bar{\mathbf{A}}$	$N_1 \times N_2 \times N_2$ tensor representation, unless specified otherwise.
$\mathbf{A^T}$ or $\mathbf{a^T}$	Transpose of a real matrix or vector $\mathbf{A}$ or $\mathbf{a}$.
$\|\mathbf{A}\|$	Frobenius norm of $\mathbf{A}$.
d, ∂, ∇	Differential, partial differential, gradient, respectively.
$\times_j (\times_1, \times_2, \ldots, \times_j)$	j-mode product of a tensor by matrix.
$\circ$	Vector outer product.
NDT	Nondestructive testing.
CM	Condition monitoring.
FD	Fault diagnosis.
SHM	Structural health monitoring.
WT	Wind turbines.
IT	Inductive thermography.
ECPT	Eddy current pulsed thermography.
OF	Optical flow.
TOF	Thermo optical flow.
μ, σ, λ	Permeability, electric conductivity, thermal conductivity, respectively.

B. Gao and J. Liu are with the School of Automation Engineering, University of Electronic Science and Technology of China, Chengdu 611731, China (e-mail: bin_gao@uestc.edu.cn; liujia617200@163.com).

Y. He is with the College of Electrical and Information Engineering, Hunan University, Changsha 410082, China, and also with the College of Mechatronics Engineering and Automation, National University of Defense Technology, Changsha 410073, China (e-mail: hejicker@163.com).

W. L. Woo is with the School of Electrical and Electronic Engineering, Newcastle University, Newcastle upon Tyne, NE1 7RU, U.K. (e-mail: lok.woo@newcastle.ac.uk).

G. Y. Tian is with the School of Automation Engineering, University of Electronic Science and Technology of China, Chengdu 611731, China, and also with the School of Electrical and Electronic Engineering, Newcastle University, Newcastle upon Tyne, NE1 7RU, U.K. (e-mail: g.y.tian@ncl.ac.uk).

Y. Hu is with the Department of Electrical Engineering and Electronics, University of Liverpool, Liverpool, L69 3BX, U.K. (e-mail: y.hu35@liverpool.ac.uk).

I. INTRODUCTION

WIND energy is one of the fastest growing renewable energy resources, and it is going to have remarkable share in the energy market [1], [2]. As the sectors of wind energy grow, business economics will demand increasingly careful management of costs. The operations and maintenance (O&M) costs of wind turbines (WTs) account for about 25–30% of the overall energy generation cost or 75–90% of the investment costs [3]. In order to reduce the cost of wind energy, there is a pressing need to reduce the O&M cost [4]. Aside from developing more advanced machine designs to improve the availability, another effective way to achieve this improvement would be to apply reliable and cost-effective condition monitoring (CM), fault diagnosis (FD), nondestructive testing (NDT) [5], and structural

Fig. 1.   Configuration of wind turbines.

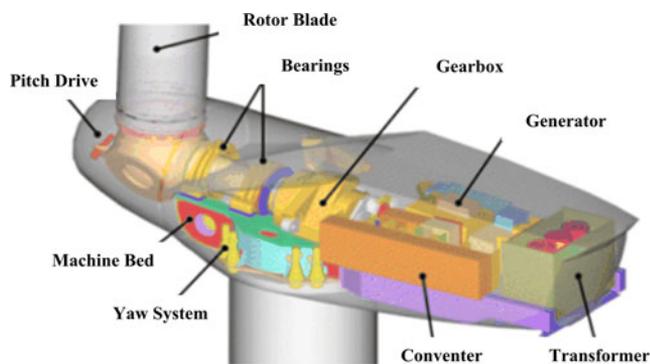Fig. 2.   Failure causes, modes and relevant CM and NDT methods for major components in wind turbine systems.

health monitoring [6], which is why this subject attracts both industrial and academic attention.

WTs are the most important systems in field of wind energy, and turbines that rotate around a horizontal axis are most common, as shown in Fig. 1. According to the location, WTs can be categorized as onshore or offshore. Onshore systems suffer fewer failures, whereas offshore turbines generate more electricity due to their larger dimensions and the stronger winds present in large open spaces without restrictions caused by the environment, noise limits and urban planning. However, the offshore WT is more expensive compared to the onshore WT [7].

The key issue in WT systems is the inherent fluctuation of winds. Variations in wind not only have a major effect on power output but also lead to sharp changes in either mechanical or electrical conditions, which are the primary causes of poor reliability and high lifecycle costs. The maintenance costs are much higher, especially for offshore turbines. Severe environments, including variation in temperature at wind farms, lighting, rain, storm, ice, etc., as well as the difficulty of access to offshore turbines, also cause high failure rates, long downtimes and expensive repair costs [8], [9]. WT is a typical mechatronics system [10], which consists of numerous mechanical and electrical components, and each of which shows independent stochastic deterioration process. Fig. 1 shows a typical structure of a geared WT, which mainly consist of blade, yaw system, bearing, gear, generator, converter, and transformer. Any component of a WT could suffer damage. From the literature survey [11], a failure map for WTs is summarized in Fig. 2, which illustrates different major critical components of WT system as well as the relevant failure causes, failure modes, and popular CM and NDT methods.

Fig. 2 indicates that faults in blades, generator, gearbox, main bearing, yaw system, and drive train have relatively long downtimes. Analytical mathematics methods, such as the Markov–Monte Carlo simulation [12], are used for modeling operating conditions and other factors. Failures are detected and characterized using NDT techniques, and subsequently the health as well as reliability of components or systems can be estimated using these analytical models. In recent years, many works in industrial electronics have been focused on CM and FD for different components of WTs [13], [14]. Mechanical faults account for a large portion of all faults in WT generators. Gong et al.
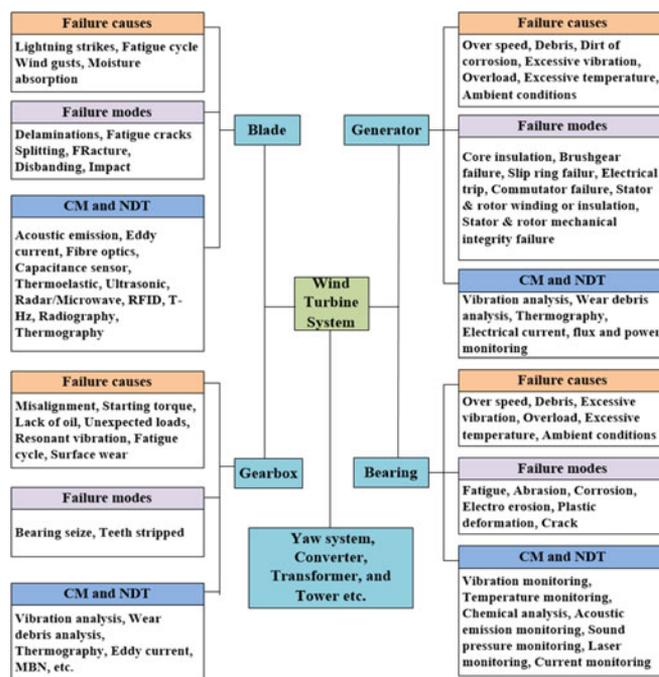
proposed a method consisting of appropriate current frequency and amplitude demodulation algorithms for bearing faults diagnosis [15]. Vedreño-Santos et al. proposed a methodology to improve the reliability of diagnosis of different types of faults in wound-rotor induction generators based on the extraction of the instantaneous frequency (IF) of the fault-related components of stator and rotor currents during speed changes caused by nonstationary functioning [16]. Gong et al. presented a computationally efficient high-resolution wideband synchronous sampling algorithm for the mechanical fault detection of variable-speed direct-drive WTs [17]. Chen et al. proposed an adaptive neuro-fuzzy inference system for machine prognosis and both cracked carrier plate and a faulty bearing are carried to validate [18]. Zhang et al. introduced a Bayesian estimation-based method to detect a fault associated with critical components/subsystems of an engineered system [19]. Kia et al. discussed the influence of transmission error, eccentricities of pinion/wheel, and teeth contact stiffness variation is demonstrated for a healthy gearbox [20]. Soualhi et al. proposed artificial ant clustering-based signal processing tool for detecting electrical and mechanical faults in the induction motors [21]. He and Yang proposed eddy current volume heating thermography and phase analysis for imaging characterization of interface delamination in CFRP blade [22].

Gears, which are known as key elements in the offshore WTs, have received significant attention in the field of CM and FD for years. Kia et al. proposed a noninvasive technique for the diagnosis of gear tooth surface damage faults based on the stator current space vector analysis [23]. Zaidi et al. proposed a prognosis method for the gear faults in dc machines, which uses the time–frequency features extracted from the motor current as machine health indicators and predicts the future state of fault severity using hidden Markov models [24]. Jae et al. proposed

a new method using a single piezoelectric strain sensor for PGB FD [25]. Du *et al.* described and analyzed a novel framework based on convex optimization, for simultaneously identifying multiple features from superimposed signals for WT gearbox FD [26]. Zhang *et al.* used the resonance residual technique for the first time to motor current signal analysis to detect planetary gearbox faults [27]. There is insufficient space to locate the sensors for long-term monitoring of fatigue state of gear, whereas the offline inspection using NDT in both manufactory and maintenance processes is critical important.

The motivation of this study mainly consists of several parts. First, the optical NDT technique such as borescope inspection is more practical on gear surface evaluation. However, borescope inspection has limitations since the inspection can only detect surface flaws but not jerkwater flaws and material degradation including stress/strain variation. In addition, it is unable to evaluate the depth of cracks [28], [29]. Therefore, it is difficult to be directly used to measure the property variation in material and identify damage prior to crack initiation while the stress redistribution variation happens in both surface and subsurface of the material in the beginning stages. Second, the scan-based eddy current and Barkhausen noise [magnetic Barkhausen noise (MBN)] are sensitive with electromagnetic property variation in materials; however, single modality of capturing the specific physics component cannot fully takes into account the complete property variation. Notwithstanding above, the scan process is slow and requires step-by-step of human intervention to control the complex geometric sample which results in the loss of efficiency and introduced unwanted interference. Third, as an emerging inspection technique, infrared (IR) thermography has become a significant tool for industrial quality control and nondestructive testing [30], [31]. Different from conventional active thermography using irradiative optical excitation (such as lamps or laser beam), inductive thermography (IT aka. eddy current pulsed thermography, ECPT) adopts high-frequency induced eddy current as an alternative thermal excitation [32], which is based on induction heating, the process of heating an electrically conducting object by electromagnetic (EM) induction and Joule heating [33]–[35]. IT has an increasing span of applications from metals to conductive composites [36]–[40]. Basic physical mechanism of IT involves Joule heating via eddy current and heat diffusion [41], [42]. These two physical phenomena are directly affected by properties variation in material, such as electrical conductivity, magnetic permeability, and thermal conductivity. In comparison with the surface heating thermography, e.g., optical excitation, the heating efficiency of inductive thermography is independence on surface condition. The heat is not limited to the sample surface, rather it can reach a certain depth, which governed by the skin depth of eddy current [43]. With conventional thermography, heating is the most commonly generated by powerful incandescent lamps and IR radiation outputted by these lamps may saturate signals during the heating time. On the contrary, little IR radiation is generated by the heating source during heating time due to the use of eddy current heating in inductive thermography [44]. Furthermore, inductive thermography focuses the heat on the defect due to friction or eddy current distortion, and subsequently increases the
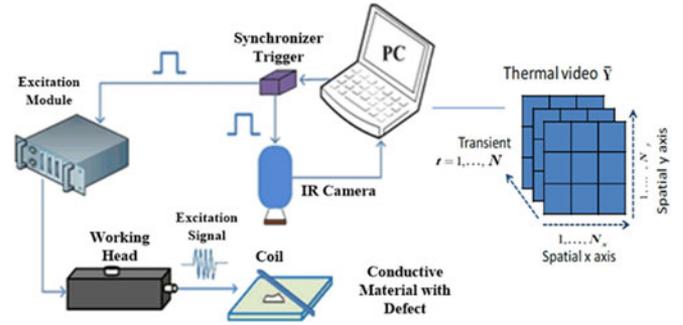

Fig. 3.   Inductive thermography diagram.

temperature contrast between the defective region and defect-free areas. Characterizing and tracking the variation of these properties are crucial as it has the potential to tackle the challenging issues such as detection and evaluation the degree of fatigue and residual stress. However, current IT characterization methods are built on the single physical field analysis. One is based on the analysis of longitudinal heat conduction from surface to subsurface in time domain [45] and frequency domain [46]. The other is based on the analysis of in-plane eddy current field perturbation [47].

In this study, inductive thermography and a physics-based multidimensional tensor model are proposed to describe the spatial-transient-stage pattern for evaluating the contact fatigue damage of offshore WT gear under different stages. This method enables information from the spatial, transient, and stage domains to be fused with the aims of characterizing and tracking the material's EM and thermal properties variation as well as evaluating the contact fatigue damage. The rest of the paper is organized as follows. The physics principle of IT and the proposed methods are introduced in Section II. Experimental setup is introduced in Section III, which is followed by results and analysis using inductive thermography and MBN in Section IV. Finally, conclusion and future work are drawn in Section V.

II. METHODOLOGY

A. Inductive Thermography

Fig. 3 shows the diagram of inductive thermography system. The excitation signal generated by the excitation module and working head is a short period of high-frequency current. It is driven to the coil on the conductive material with defect. Then, the current in the coil will induce the eddy currents and generate the resistive heat in the conductive material. The heat will diffuse in time until that it reaches equilibrium in the material. If there is a defect (e.g., crack) in the conductive material, eddy current distribution or heat diffusion process will vary from that of sound area. Consequently, the spatial distribution of temperature on the surface of material and the temperature transient response over time will show the variation, which is captured by an IR camera [41], [42]. However, for nonapparent defect such as fatigue, it is difficult to determine the abnormal features from only the temperature spatial distribution and transient response. Instead, it requires the fusion of the spatial, transient, and the

information of fatigue stage in order to characterize and track the weak property variation.

The IR camera records both spatial and transient responses of temperature variation on the specimen. This can be represented as a spatial-transient tensor $\bar{\mathbf{Y}}$ which has dimension $\underbrace{N_x \times N_y}_{\text{Spatial}} \times \underbrace{N}_{\text{Transient}}$. The governing equation describing the EM field in the ECPT system can be deduced from Maxwell's equations, for time-varying fields [18], namely,

$$\sigma \frac{\partial A}{\partial t} + \nabla \times \left(\frac{1}{\mu} \nabla \times A \right) - \sigma v \times (\nabla \times A) = \sigma \frac{V_{\text{loop}}}{2\pi r} + J \tag{1}$$

where μ is the permeability of the inspected specimen; $J_s = \sigma(\partial A/\partial t)$ denotes the eddy current density J_s; J is the excitation source current density; V_{loop} is the loop potential; r is the loop radius; and $v = (\mu\varepsilon)^{-1/2}$ is the wave velocity in media. When an EM field is applied to a conductive material, the temperature increases owing to resistive heating from the induced electric current which is known as Joule heating. The sum of the generated resistive heat Q is proportional to the square of the magnitude of the electric current density. Current density, in turn, is proportional to the electric field intensity vector E. The following equation expresses this relationship:

$$Q = \frac{1}{\sigma} |J_s|^2 = \frac{1}{\sigma} |\sigma E|^2 \text{ where } \sigma = \frac{\sigma_0}{1 + \alpha(T - T_0)} \tag{2}$$

where electric conductivity σ is dependent on temperature and σ_0 is the conductivity at the reference temperature T_0 and α is the temperature coefficient of resistivity, which describes how resistivity varies with temperature. In general, by taking account of heat diffusion and Joule heating [19], the heat conduction equation of a specimen can be expressed as:

$$\frac{\partial T}{\partial t} = \frac{\lambda}{\rho C_p} \left(\frac{\partial^2 T}{\partial x^2} + \frac{\partial^2 T}{\partial y^2} + \frac{\partial^2 T}{\partial z^2} \right) + \frac{1}{\rho C_p} q(x, y, z, t) \tag{3}$$

where $T = T(x, y, z, t)$ is the temperature distribution, λ is the thermal conductivity of the material (W/m·K), which is dependent on temperature. ρ is the density (kg/m³), C_p is specific heat (J/kg·K). $q(x, y, z, t)$ is the internal heat generation function per unit volume, which is the result of the eddy current excitation. The variation of temporal temperature depends on the spatial temperature variation for heat conduction. The heat diffusion rate increases along with the increased temperature as difference between $T(x, y, z, t)$ in (x, y, z) and all other locations round about it (environment). In general, the thermal conductivity λ decreases as $T(x, y, z, t)$ variation increases for pure metal material and the eddy current generates Joule heating denoted as $q(x, y, z, t)$ According to (1) and (3), heat conduction is influenced by $T(x, y, z, t), \xi, \theta, \sigma, \mu,$ and l. From the above analysis, it is known that the variation of temperature spatial and transient response recorded from IR camera directly reflects the internal properties variation of material.

According to (2) and (3), the generated resistive heat Q has a relationship with electric conductivity and permeability. In addition, heat conduction has a relationship with thermal conductivity, density and specific of material. From above analysis, it is known that the variation of spatial and transient temperature captured by IR camera contains information of internal property variations [41], [42].

B. Thermal Optical Flow (TOF) Modeling

During early stage of the contact fatigue process, microdefect such as dislocations (point-defects in the crystal lattice) and the organization of the dislocations in substructures (cells, cell bundles, etc.) play an important role that directly influence the conductive material property. These properties variation directly affect both spatial and transient thermal patterns. However, as they are nonapparent defects, traditional defect evaluation methods such as pixel selection cannot obtain reliable solution. Optical flow (OF) is a powerful tool to estimate velocity fields and track small target object [48]. In this study, OF is modeled as TOF to characterize the heating flow between the adjacent thermography frames and to identify and evaluate the region suffering from contact fatigue damage. TOF is calculated to trace motion between two thermal images captured at times t and $t + \Delta t$. The intensity is defined as $O(x, y, t) = O(x + \Delta x, y + \Delta y, t + \Delta t)$, the image constraint at $O(x, y, t)$ with the Taylor series can be developed to

$$O(x + \Delta x, y + \Delta y, t + \Delta t) = O(x, y, t) + \ldots \frac{\partial O}{\partial x} \Delta x$$
$$+ \frac{\partial O}{\partial y} \Delta y + \frac{\partial O}{\partial t} \Delta t + \ldots o(\Delta x^2 + \Delta y^2 + \Delta t^2). \tag{4}$$

Following the definition of intensity, (4) will lead to $\frac{\partial O}{\partial x} v_x + \frac{\partial O}{\partial y} v_y + \frac{\partial O}{\partial t} v_t = 0$ where v_x and v_y are the x and y components of the velocity or optical flow of $O(x, y, t)$ and $\partial O/\partial x, \partial O/\partial y$ and $\partial O/\partial t$ are the derivatives of the image at (x, y, t) in the corresponding directions. Since the intensity $O(x, y, t)$ is captured by the IR camera [49], the relationship between the intensity $O(x, y, t)$ and the temperature T is related as $O(x, y, t) \propto T$. The first derivative with respect to time t is given as $\frac{\partial O}{\partial t} \propto \frac{\partial T}{\partial t}$, therefore, (4) with x- and y-direction can be derived as follows:

$$-\frac{\partial T}{\partial t} \propto \frac{\partial O}{\partial x} v_x + \frac{\partial O}{\partial y} v_y. \tag{5}$$

Thus, (5) establishes relationship between TOF and the rate of temperature change. The two key parameters v_x and v_y are used to characterize the spatial and the transient of the thermal flow, the formula (5) in which there are two unknowns and the Horn–Schunck method is used for the estimation, where the flow is formulated as a global energy functional which is solved through minimization $\overrightarrow{F} = [\mathbf{v}_x, \mathbf{v}_y]^{\mathbf{T}}$ is the TOF vector, and superscript "$\mathbf{T}$" denotes the transpose

$$E = \iint \left[\left(\frac{\partial O}{\partial x} v_x + \frac{\partial O}{\partial y} v_y + \frac{\partial O}{\partial t} \right)^2 + \alpha^2 \left(|\nabla v_x|^2 + |\nabla v_y|^2 \right) \right] d_x d_y. \tag{6}$$

In (6), the smoothness weight $\alpha > 0$ serves as a regularization parameter: Larger values for α result in a stronger penalization of large flow gradients and lead to smoother flow fields. Due
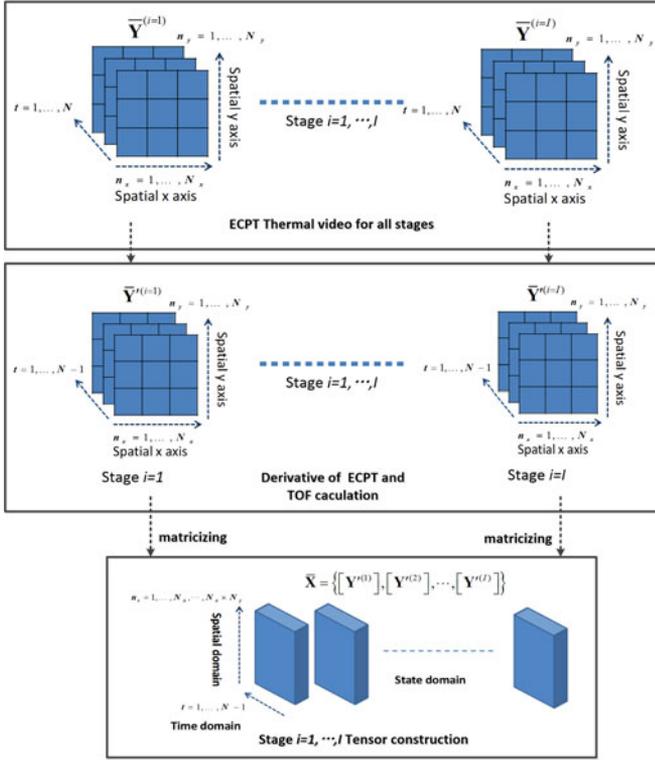
Fig. 4. Flow diagram of spatial-transient-stage tensor construction.

Fig. 5. Illustration of matricizing operation of $\bar{\mathbf{Y}}\prime^{(i)}$.

to the Horn–Schunck algorithm being an ill-posed problem, the value of v_x and v_y is estimated and the specific steps are summarized in [22].

C. Integration of TOF and Tensor Modeling

Besides TOF, this study introduces another key pattern denoted as stage domain of fatigue. As fatigue loading cycles increase, the degree of contact fatigue damage inevitably increases. This information can be fused with TOF to construct the spatial-transient-stage model. More specifically, let $i = 1, \ldots, I$ denote ith stage. Take gear fatigue test as an example, in stage 1, we perform ECPT on a completely new gear; after that, the new gear will run a certain number of cycles (e.g., 8×10^6) and the contact part of gear will be inevitably suffered from fatigue (the material property electrical conductivity, magnetic permeability, and thermal conductivity of the contact part will be different from the completely new one), the ECPT will be conducted on this gear and this is considered as stage 2. Notwithstanding this, we continue running this gear for another 8×10^6 cycles which will be denoted as stage 3, and so on. For each stage i, TOF tensor is denoted as $\bar{\mathbf{Y}}\prime^{(i)}$ and it corresponds to property variation of $\theta_i = \{\sigma_i, \lambda_i, \mu_i\}$. TOF for each stage containing velocity in both x- and y-direction is given by $\bar{\mathbf{Y}}\prime = \{\mathbf{v}_x, \mathbf{v}_y\}$. Supposing we totally have I stages, the specific steps of spatial-transient-stage tensor can be constructed as shown in Figs. 4 and 5.

In Fig. 4, the ith stage TOF calculation of ECPT thermal video $\bar{\mathbf{Y}}^{(i)}\%$ is denoted as $\bar{\mathbf{Y}}\prime^{(i)}$ and it corresponds to property variation of $\theta_i = \{\sigma_i, \lambda_i, \mu_i\}$, $\bar{\mathbf{Y}}\prime^{(i)}$ can be transformed
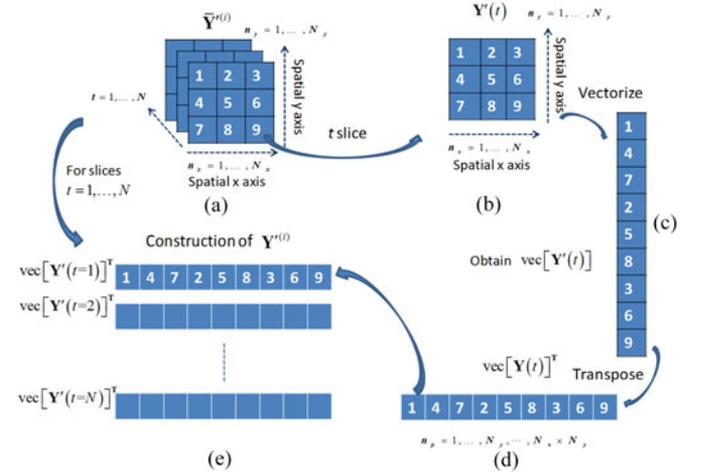
into a matrix $\mathbf{Y}\prime^{(i)}$ which has dimension $L \times (N - 1)$, where $L = N_x \times N_y$, the specific procedure of transform is explained in Fig. 5(a)–(e). The symbol $\text{vec}[\bullet]$ denotes vectorization operation. Finally, once $i = 1, \ldots, I$ stages ECPT thermal videos have been transformed, the spatial-transient-state tensor representation $\bar{\mathbf{X}} = \{[\mathbf{Y}\prime^{(1)}], [\mathbf{Y}\prime^{(2)}], \ldots, [\mathbf{Y}\prime^{(I)}]\}$ can be formed straightforwardly. The richness of information obtained from this construction enables the fusion of the all the ith material properties θ_i whose variations are revealed in the spatial, transient, and stage domain. Subsequently, all domains are combined to characterize and track the θ_i in order to improve the robustness and remove ambiguities in any single domain. When θ_i varies, based on (1) and (2), these variations will affect both heat diffusion and flow velocity.

Therefore, under the assumption that the spatial, transient, and stage features within the property variation regions are different from those which are not affected, the multidimensional canonical decomposition [50] of spatial-transient-stage tensor $\bar{\mathbf{X}} \in R^{L \times N_T \times I}$ where $N_T = N - 1$ will provide us with the "basis patterns" that correspond to the spatial domain (to locate the region whose θ_i varies), transient domain (to determine how the signal within these region propagate in time series), and stage domain (to determine how much degree of θ_i change within these regions at ith stage). This gives

$$\bar{\mathbf{X}} = \bar{\mathbf{g}} \times_1 \mathbf{A} \times_2 \mathbf{B} \times_3 \mathbf{C} = \sum_{p=1}^{P} \sum_{q=1}^{Q} \sum_{r=1}^{R} g_{\mathrm{pqr}} \mathbf{a}_p \circ \mathbf{b}_q \circ \mathbf{c}_r$$

(7)

where $\mathbf{A} \in \Re^{L \times P}$, $\mathbf{B} \in \Re^{N_T \times Q}$, and $\mathbf{C} \in \Re^{I \times R}$ are factor basis matrix of spatial, transient, and stage, respectively; $\mathbf{a}_j \in \Re^L$, $\mathbf{b}_j \in \Re^{N_T}$, and $\mathbf{c}_j \in \Re^I$ are factor basis vector of spatial, transient, and stage, respectively,. The symbol "$\circ$" represents the vector outer product and the steps of decomposition and $\bar{\mathbf{g}} \in \Re^{P \times Q \times R}$ is the core tensor and its entries show the level of interaction between the different components. Here P, Q, and R are the number of components (i.e., columns) in the factor matrices. "$\circ$" represents the vector outer product. The estimation of the factor basis and core tensor is given by the following
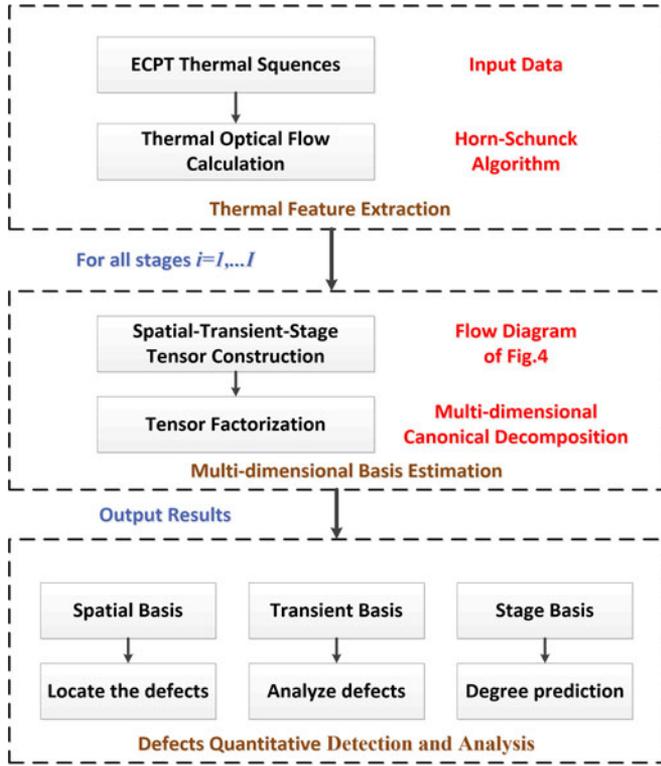
Fig. 6.   Flow diagram of the proposed method.

Fig. 7.   (a) ECPT experimental system, (b) explanation of gear teeth and the coil placement, and (c) fatigue test gear with inductor coil.

optimization problem:

$$\min_{\bar{\mathbf{Z}}} \left\| \bar{\mathbf{X}} - \bar{\mathbf{Z}} \right\| \quad \text{with} \quad \bar{\mathbf{Z}} = \sum_{p=1}^{P} \sum_{q=1}^{Q} \sum_{r=1}^{R} g_{\mathrm{pqr}} \mathbf{a}_p \circ \mathbf{b}_q \circ \mathbf{c}'_r \tag{8}$$

where $\| \bullet \|$ is the matrix Frobenius norm which is defined as

$$\left\| \bar{\mathbf{X}} \right\| = \sqrt{\sum_{i_1}^{I_1} \sum_{i_2}^{I_2} \cdots \sum_{i_N}^{I_N} x^2_{i_1, i_2 \dots, i_N}}' \tag{9}$$

The specific update procedure to estimate factor basis and core tensor can be found in [30], [31], and [34]. The flow diagram of the proposed method is summarized in Fig. 6. It mainly consists of 1) given the input stage ECPT video sequences $\bar{\mathbf{Y}}^{(i)}$ and calculate its corresponding TOF $\bar{\mathbf{Y}}'^{(i)}$ for $i = 1, \dots, I$. 2) Tensor construction of $\bar{\mathbf{X}} = \{[\mathbf{Y}'^{(1)}], [\mathbf{Y}'^{(2)}], \cdots, [\mathbf{Y}'^{(I)}]\}$ and basis factorization using canonical decomposition are carried out. 3) The analysis of spatial, transient, and stage basis is conducted.

III. EXPERIMENTAL SETUP

ECPT experiment platform was built as shown in Fig. 7(a). A SC7500 IR camera was used for capturing the temperature field, which is a Stirling cooled camera with a 320×256 array of 1.5–5 μm InSb detectors and has a sensitivity of <20 mK and a maximum full frame rate of 383 Hz. A rectangular coil was constructed to apply directional excitation, which is made of 6.35-mm high conductivity hollow copper tubing. The radiation of the object was sampled using the commercial thermography software Altair and the unit of radiation is digital level (DL). A nonlinear transfer function after calibration can convert the
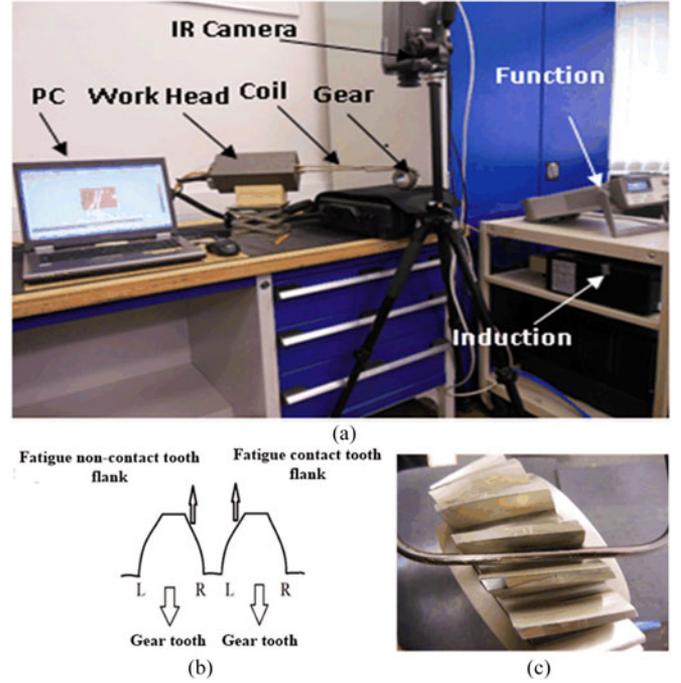
radiation (unit: DL) into temperature (unit: K), which requires an operator setting several parameters (emissivity, background temperature, transmission, etc.). We used DL as the unit of temperature in experimental studies. As shown in Fig. 7(b) and (c), the 6-mm module helical test gear with a 44-mm face width was tested which manufactured from 18CrNiMo7 steel bar. The gears were tested on a 160-mm center distance back-to-back contact fatigue test rig at 3000 r/min (pinion) with BAG oil at 90 °C. A stepwise micropitting test involves running gears at incrementally increasing contact stress levels with each stage running for up to 8×10^6 cycles and totally has seven stages [51]. This is shown in Fig. 8. 8×10^6 cycles take the running for 44.44 h, which takes approximately 160×10^3 s.

IV. EXPERIMENTAL RESULTS AND ANALYSIS

A. Inductive Thermography and Tensor

In IT experiments, 2 s video were recorded by camera which includes 400-ms heating time followed by 1600 ms cooling time. The spatial patterns of gear with 40×10^6 cycles (stage 5) at 0.2 s are shown in Fig. 9(a). Micropitting and wear occurred on contact surface during fatigue running, which can cause a variation in spatial and transient of temperature [52]. Fig. 9(b) shows TOF results of gear with 40×10^6 cycles. The size and direction of arrows indicate the value and direction of TOF, respectively. During the transformation of retained austenite into martensite and fatigue softening, permeability increases as the number of cycles increase. After a certain number of cycles, dislocations accumulation will manifest which lead to a decrease in thermal conductivity and electrical conductivity [52]. The variation in material properties is very weak and fatigue is not manifested by
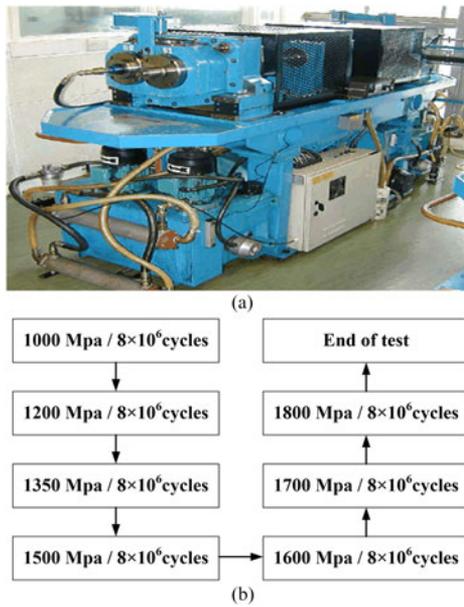
Fig. 8. (a) 160 mm center distance back-to-back contact fatigue test rig facility at Design Unit, Newcastle University, (b) procedure of the stepwise fatigue test (8 × 106 cycles takes the running for 44.44 h).
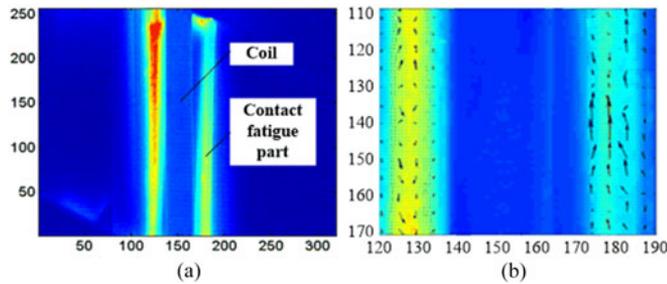

Fig. 9. (a) Raw thermal image at 0.2 s. (b) Thermo optical flow (room in region).

one or several impact points but it directly affects a certain area. Thus, it is extremely difficult to obtain temperature variation information from Fig. 9(a). By deriving TOF, it is clear to see TOF have uniform distribution and order direction at the noncontact tooth flank since the microstructure does not vary. Specifically, due to the property variation during the fatigue process, singular patterns of TOF appear at fatigue contact tooth flank and TOF converge on the fatigue affective areas. This is reflected by size and direction of arrows. However, TOF only considers spatial and transient information but ignores stage information.

The proposed TOF-stage tensor and decomposition will tackle on all seven stages of IT data. The jointly estimated factor basis $\{a_j, b_j, c_j\}$ is more precise as they are optimized under a more complete dataset rather than individual dataset from different stages. Fig. 10 validates the decomposition method which shows the potential to characterize and track the variation of gear fatigue evolution. In Fig. 10(a), the spatial basis captures the singular regions at the fatigue contact teeth. The tensor model enables a more accurate and consistent inference due to the influenced factors rather than the individual process. Fig. 10(b) shows the transient basis where it directly displays the
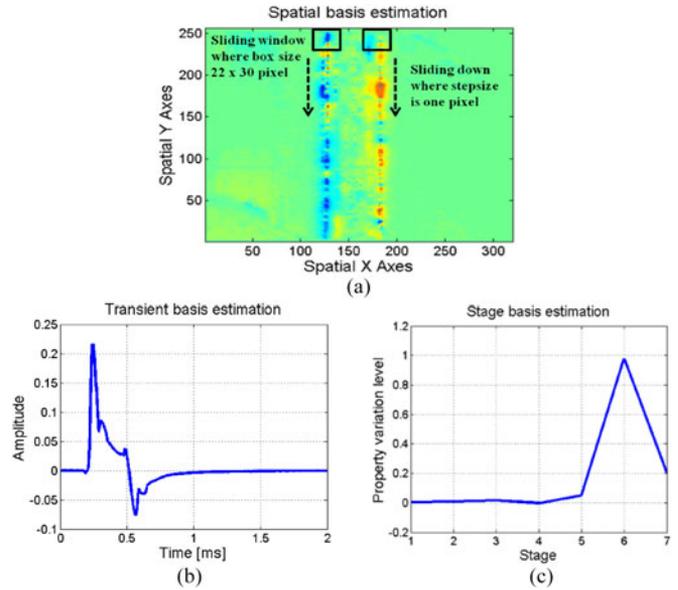

Fig. 10. The decomposition results for gear fatigue test: (a) Spatial basis, (b) transient basis, and (c) stage basis.

characteristic of heat conduction. It also shows that it has the potential being a classifier for multidefects recognition. Fig. 10(c) shows the factorized stage basis and it is directly used to predict the degree of fatigue during the different stages. The stage basis implies that the material property varies more obviously with the increase of number of fatigue circles and derives the correlation results [52]. Specifically, the estimated stage basis retains a consistent ratio in the first three stages, but fluctuates in stages four and five which resulted as accumulation of multifactor and, then, sharply increases at the six stage. During the early cyclic deformation, only a few grains are plastically deformed and the deformation degrees are different. With the increase of fatigue cycle, both number and degrees of deformed grains also increase. Once these reach a certain level, the property varies sharply. This explains the sudden increase of stage basis at the stages 6 and 7. These have been validated using Barkhausen noise (MBN) in next section.

In order to reflect the changes of TOC in specific spatial domain, the mean of TOC is extracted. This has been done by using a sliding window to analyzing the mean of TOC within a small region for both contact and noncontact fatigue tooth where the size of the window is 22 by 30 pixel and step size is 1 pixel along the Y-coordinate.. This is shown in Fig. 11. The size of the sliding window exactly coincides with the size of the measured gear teeth. The mean value indicates the degree of the TOC which directly associates with the level of fatigue.

From Fig. 11(a), the mean of TOC became obviously different for the two teeth. The value (blue dash line) in overall is greater on the fatigue contact tooth flank. As the heat distribution is uniform at fatigue noncontact tooth flank, the degree of TOF is lower. At the fatigue contact tooth flank, the heat converges at the places where the singular values of TOF appeared because of the changing microstructure on the fatigue contact tooth flank surface. As the TOF value is quite different between
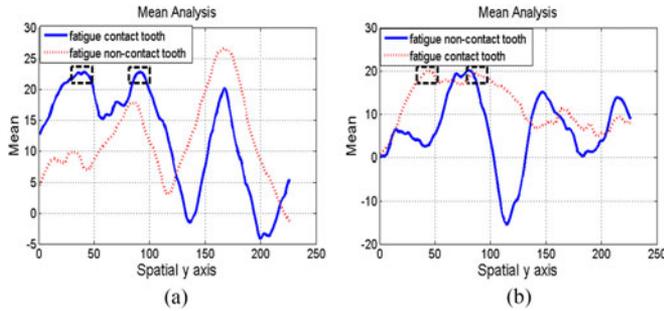
Fig. 11. (a) Mean of TOF stage basis by using sliding window; (b) validation experiments which fatigue contact tooth flank on the left side.
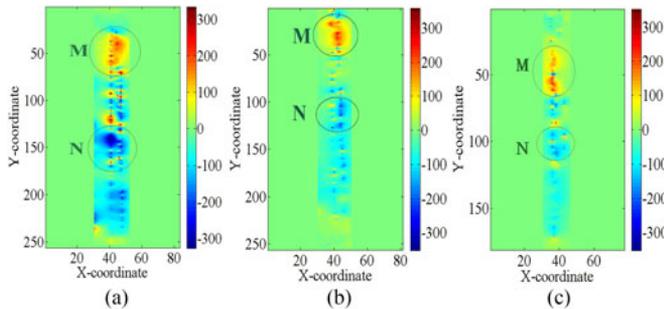

Fig. 12. 2-D pseudocolor images of TOC at different stages: (a) at stage 7; (b) at stage 5; and (c) at stage 3.

the area where the heat converges and the adjacent area, the degree is higher. To validate this finding, we have done the repeat experiment which put the fatigue contact tooth on the left side and do the ECPT for all stages, Fig. 11(b) shows the mean of TOF stage basis by using sliding window where it (red dot line) confirm the results. Notwithstanding above, it is found that the black-box marked region has prominent characteristic.

Fig. 12 shows the TOF of stage 7, stage 5, and stage 3, respectively. There exist singular values of TOF at M and N areas (black box marked region in Fig. 11). During the early cyclic deformation, only some of the grains are plastically deformed and the plastic deformation degrees of the grains are different. With increasing fatigue cycles, the extent of plastic deformation of the grains increases and the number of grains which are plastically deformed is also increased. This explains that fatigue damage of the material structure suddenly increases in M and N areas. The areas M and N can be considered as an incubation area of a fatigue crack, where physical characteristics are significantly changed in these areas. Furthermore, the fatigue damage is diffused from M and N areas to the surroundings and fatigue damage appears across the whole area of the fatigue contact tooth flank.

B. Validation Study by Using Barkhausen Noise

In a ferromagnetic material, Barkhausen noise is generated by the discontinuous movement of irreversible domain walls. This noise can be detected in the form of voltage pulses which are induced in a coil placed near the surface of the material, called MBN. MBN is expected as a useful way of detecting nonappar-
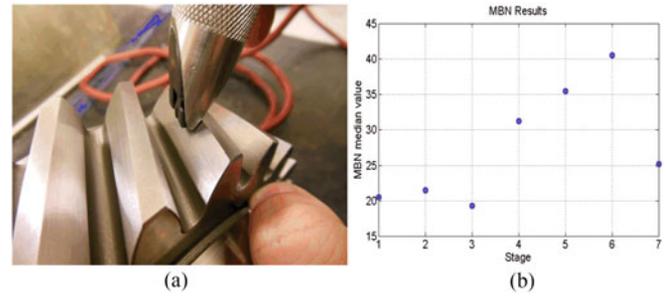

Fig. 13. (a) MBN experiment and (b) results in a specific location.

ent defects such as fatigue or residual stress. Govindaraju *et al.* used the MBN for identifying the fatigue softening, saturation, crack propagation stages during low-cycle fatigue in medium strength steel. Moorthy *et al.* investigated evaluation of contact fatigue damage and bending fatigue on gears using MBN [53]–[55]. The high-frequency MBE measurements have been made using the commercially available u-Scan/Rollscan 500-2 system supplied by Stress technology, Finland. A standard flat-surface probe with a ferrite-cored electromagnet with a pole gap distance of 3 mm and a ferrite-cored MBE pickup fixed at the center of the pole gap has been used. They have shown that both MBN peak and profile can be used to assess the various stages of deformation and fracture during the fatigue propagation. According to these works, Fig. 13 (Moorthy's work) indicates that root mean square (RMS) variation of MBN is faint at the initial stage because of small variation in gear material (first stage). After a certain number of cycles, the RMS value increases as the cycles increase, which is attributed to the combined effects of deformation induced transformation of retained austenite into martensite and fatigue softening. However, when number of cycles reaches 45 million (seven stages), this results in 1) plastic deformation induced formation of more compressive residual stresses and cyclic hardening of the microstructure; 2) the transformation of retained austenite to martensite would be completed; and 3) additional dislocations would be generated which cause decrease in the displacement length of magnetic domain walls. These have contributed to the decrease in the MBN level from maximum [53]–[55]. Further clarification including measurement location supervised by the proposed method TOF will be considered.

Three scan line with five measurement points are measured tooth surface, including addendum, root of tooth, and middle line tooth. The experiment is shown in Fig. 13(a) and takes the median value of the all tested points. Fig. 13(b) shows the MBN results for all seven stages. Analyzing the results, there exist highly correlation between MBN results with tensor decomposition stage basis in Fig. 10(c) and the correlation coefficient is 70% while both results display the similar trend of variation level with progressive number of cycles. However, the MBN technique requires scan process step by step and humanly controlling for complex geometric sample. This will result less efficiency and unwanted interference. The ECPT can overcome this because the heat of ECPT is not limited to the sample surface and can image a large area within short time.

C. Advantages and Limits

Inductive thermography is a NDT method that combines eddy current testing (ECT), magnetic testing and thermography. Its advantages include speed of processing, providing noncontact, noninteraction, real-time measurements over a large detection area with long range, and exploiting the EC characteristic that is sensitive to surface small defects. The advantages of inductive thermography over conventional thermography with optical excitation have been discussed in Section I. In comparison with ECT and MBN, it does not require the step-by-step scanning process and human intervention for controlling the complex geometric sample which will result substantial loss of efficiency and introduced unwanted interference.

Several signal processing methods have been investigated in inductive thermography, such as thermal transient selection, thermographic signal reconstruction based on logarithm domain transform [56], phase analysis in frequency domain [22], gradient analysis based on lateral heat conduction [57], principal component analysis, and independence component analysis [41]. These methods have shown great potentials on finding the defects. However, if the hidden defects exist (e.g., fatigue) where sample is under property variation, it is difficult to find the abnormal features from the temperature spatial distribution only but require the fusion of different domain information in order to characterize and track the property variation. The proposed method fuses three domain types, i.e., spatial, transient, and stage. It also bridges the physics and mathematical model to tackle the weak variation of thermal characteristic of hidden defects and validate its efficiency.

The limitation of the proposed method is that the advantages gained by the proposed methods are augmented by high cost of instrumentation platform and the increase of computational power and higher data storage requirements of the processors. In our implementation, a high-specification computer with a PC server with of Core i7 64-GB RAM is required to implement the data and algorithm.

V. Conclusion

In this paper, a physics-based multidimensional tensor model with the help of inductive thermography has been proposed. The model describes the spatial-transient-stage pattern for subsequent evaluation of the contact fatigue damage in WT gear. The model has been verified by experimental studies where real gears with different cycles of contact fatigue are tested. First, through TOF, material property variation has been linked to multiple physical fields involving Joule heating and heat diffusion. The spatial-transient-stage tensor construction model and multidimensional decomposition algorithm are then proposed for characterizing and tracking the property variation from multiple stages. From obtained results, conclusion can be drawn as follows: 1) The estimated spatial basis emphasizes the property variation which can be further used for detecting the affected region; 2) the stage basis directly reflects the variation of each property and can be used to track the degree of variation during the fatigue procedure. Future study will be conducted to minimize several affective factors during the ECPT experiment such

as emissivity, liftoff, geometric shape, and environment. The proposed methods can be exploited for emerging in-situ applications such as high-speed railway and nuclear plants for fast imaging, localization, visualization, and evaluation. In addition, the gear fatigue damage at lower than 1 Hz rotating speed is much more valuable than 50 Hz. As this is the initial research work, the first step is to evaluate how the property variation and look for insight of what exactly material property varies during the fatigue process. Further study will carry out the fatigue evaluation at 1 Hz rotating speed.

References

[1] H. Sanchez, T. Escobet, V. Puig, and P. F. Odgaard, "Fault diagnosis of an advanced wind turbine benchmark using interval-based ARRs and observers," *IEEE Trans. Ind. Electron.*, vol. 62, no. 6, pp. 3783–3793, Jun. 2015.

[2] S. Chuangpishit, A. Tabesh, Z. Moradi-Shahrbabak, and M. Saeedifard, "Topology design for collector systems of offshore wind farms with pure DC power systems," *IEEE Trans. Ind. Electron.*, vol. 61, no. 1, pp. 320–328, Jan. 2014.

[3] M. de Prada Gil, O. Gomis-Bellmunt, and A. Sumper, "Technical and economic assessment of offshore wind power plants based on variable frequency operation of clusters with a single power converter," *Appl. Energy*, vol. 125, pp. 218–229, Jul. 15, 2014.

[4] S. Simani, S. Farsoni, and P. Castaldi, "Fault diagnosis of a wind turbine benchmark via identified fuzzy models," *IEEE Trans. Ind. Electron.*, vol. 62, no. 6, pp. 3775–3782, Jun. 2015.

[5] R. Yang, Y. He, and H. Zhang, "Progress and trends in nondestructive testing for wind turbine composite blade," *Renewable Sustain. Energy Rev.*, vol. 60, pp. 1225–1250, 2016.

[6] M. Moradi and S. Sivoththaman, "MEMS multisensor intelligent damage detection for wind turbines," *IEEE Sensors J.*, vol. 15, no. 3, pp. 1437–1444, Mar. 2015.

[7] M. Drewry and G. Georgiou, "A review of NDT techniques for wind turbines," *Insight*, vol. 49, no. 3, pp. 137–141, 2007.

[8] S. Saleh, R. Ahshan, and C. Moloney, "Wavelet-based signal processing method for detecting ice accretion on wind turbines," *IEEE Trans. Sustain. Energy*, vol. 3, no. 3, pp. 585–597, Jul. 2012.

[9] A. Candela Garolera, K. L. Cummins, S. F. Madsen, J. Holboell, and J. D. Myers, "Multiple lightning discharges in wind turbines associated with nearby cloud-to-ground lightning," *IEEE Trans. Sustain. Energy*, vol. 6, no. 2, pp. 526–533, Apr. 2015.

[10] S. Yin, X. Li, H. Gao, and O. Kaynak, "Data-based techniques focused on modern industry: An overview," *IEEE Trans. Ind. Electron.*, vol. 62, no. 1, pp. 657–667, Jan. 2014.

[11] Z. Hameed, Y. S. Hong, Y. M. Cho, S. H. Ahn, and C. K. Song, "Condition monitoring and fault detection of wind turbines and related algorithms: A review," *Renewable Sustain. Energy Rev.*, vol. 13, no. 1, pp. 1–39, Jan. 2009.

[12] D. McMillan and G. W. Ault, "Condition monitoring benefit for onshore wind turbines: Sensitivity to operational parameters," *IET Renewable Power Gener.*, vol. 2, no. 1, pp. 60–72, 2008.

[13] Y. Gritli *et al.*, "Advanced diagnosis of electrical faults in wound-rotor induction machines," *IEEE Trans. Ind. Electron.*, vol. 60, no. 9, pp. 4012–4024, Sep. 2013.

[14] J. Blesa, P. Jimenez, D. Rotondo, F. Nejjari, and V. Puig, "An interval NLPV parity equations approach for fault detection and isolation of a wind farm," *IEEE Trans. Ind. Informat.*, vol. 62, no. 6, pp. 3794–3805, May 2015.

[15] X. Gong and W. Qiao, "Bearing fault diagnosis for direct-drive wind turbines via current-demodulated signals," *IEEE Trans. Ind. Electron.*, vol. 60, no. 8, pp. 3419–3428, Aug. 2013.

[16] F. Vedreno-Santos, M. Riera-Guasp, H. Henao, M. Pineda-Sánchez, and R. Puche-Panadero, "Diagnosis of rotor and stator asymmetries in wound-rotor induction machines under nonstationary operation through the instantaneous frequency," *IEEE Trans. Ind. Electron.*, vol. 61, no. 9, pp. 4947–4959, Sep. 2014.

[17] X. Gong and W. Qiao, "Current-based mechanical fault detection for direct-drive wind turbines via synchronous sampling and impulse detection," *IEEE Trans. Ind. Electron.*, vol. 62, no. 3, pp. 1693–1702, Mar. 2014.

[18] C. Chen, B. Zhang, G. Vachtsevanos, and M. Orchard, "Machine condition prediction based on adaptive neuro-fuzzy and high-order particle filtering," *IEEE Trans. Ind. Electron.*, vol. 58, no. 9, pp. 4353–4364, Sep. 2011.

[19] B. Zhang *et al.*, "A probabilistic fault detection approach: Application to bearing fault detection," *IEEE Trans. Ind. Electron.*, vol. 58, no. 5, pp. 2011–2018, May 2011.

[20] S. H. Kia, H. Henao, and G. A. Capolino, "Torsional vibration effects on induction machine current and torque signatures in gearbox-based electromechanical system," *IEEE T. Ind. Electron.*, vol. 56, no. 11, pp. 4689–4699, 2009.

[21] A. Soualhi, G. Clerc, and H. Razik, "Detection and diagnosis of faults in induction motor using an improved artificial ant clustering technique," *IEEE Trans. Ind. Electron.*, vol. 60, no. 9, pp. 4053–4062, Sep. 2013.

[22] Y. He and R. Yang, "Eddy current volume heating thermography and phase analysis for imaging characterization of interface delamination in CFRP," *IEEE Trans. Ind. Informat.*, vol. 11, no. 6, pp. 1287–1297, Dec. 2015.

[23] S. H. Kia, H. Henao, and G. A. Capolino, "Gear tooth surface damage fault detection using induction machine stator current space vector analysis," *IEEE Trans. Ind. Electron.*, vol. 62, no. 3, 1866–1878, Mar. 2015.

[24] S. S. H. Zaidi, S. Aviyente, M. Salman, S. Kwang-Kuen, and E. G. Strangas, "Prognosis of gear failures in DC starter motors using hidden markov models," *IEEE Trans. Ind. Electron.*, vol. 58, no. 5, pp. 1695–1706, May 2011.

[25] Y. Jae, D. He, and B. Van Hecke, "On the use of a single piezoelectric strain sensor for wind turbine planetary gearbox fault diagnosis," *IEEE Trans. Ind. Electron.*, vol. 62, no. 10, pp. 6585–6593, Oct. 2015.

[26] J. Zhang, J. S. Dhupia, and C. J. Gajanayake, "Stator current analysis from electrical machines using resonance residual technique to detect faults in planetary gearboxes," *IEEE Trans. Ind. Electron.*, vol. 62, no. 9, pp. 5709–5721, Sep. 2015.

[27] Z. Du, X. Chen, H. Zhang, and R. Yan, "Sparse feature identification based on union of redundant dictionary for wind turbine gearbox fault diagnosis," *IEEE Trans. Ind. Electron.*, vol. 62, no. 10, pp. 6594–6605, Oct. 2015.

[28] M. Trimm, "An overview of nondestructive evaluation methods," *J. Failure Anal. Prev.*, vol. 3, no. 3, pp. 17–31, 2003.

[29] Anon, "Video borescoping helps keep gas turbines healthy," *Turbomach. Int.*, vol. 39, no. 5, pp. 46–48, 1998.

[30] S. Stipetic, M. Kovacic, Z. Hanic, and M. Vrazic, "Measurement of excitation winding temperature on synchronous generator in rotation using infrared thermography," *IEEE Trans. Ind. Electron.*, vol. 59, no. 5, pp. 2288–2298, May 2012.

[31] D. M. Tsai, S. C. Wu, and W. Y. Chiu, "Defect detection in solar modules using ICA basis images," *IEEE Trans. Ind. Informat.*, vol. 9, no. 1, pp. 122–131, Feb. 2013.

[32] B. Gao, W. L. Woo, Y. He, and G. Y. Tian, "Unsupervised sparse pattern diagnostic of defects with inductive thermography imaging system," *IEEE Trans. Ind. Informat.*, vol. 12, no. 1, pp. 371–383, Feb. 2015.

[33] V. Esteve *et al.*, "Improving the reliability of series resonant inverters for induction heating applications," *IEEE Trans. Ind. Electron.*, vol. 61, no. 5, pp. 2564–2572, May 2014.

[34] O. Lucia, P. Maussion, E. J. Dede, and J. M. Burdio, "Induction heating technology and its applications: past developments, current technology, and future challenges," *IEEE Trans. Ind. Electron.*, vol. 61, no. 5, pp. 2509–2520, May 2014.

[35] O. Lucia, P. Maussion, E. J. Dede, and J. M. Burdio, "Introduction to the special section on induction heating systems," *IEEE Trans. Ind. Electron.*, vol. 61, no. 5, pp. 2504–2508, May 2014.

[36] B. Gao, L. Bai, and W. L. Woo, "Thermography pattern analysis and separation," *Appl. Phys. Lett.*, vol. 104, no. 25, 2014, Art. no. 251902.

[37] R. Yang and Y. He, "Eddy current pulsed phase thermography considering volumetric induction heating for delamination evaluation in carbon fiber reinforced polymers," *Appl. Phys. Lett.*, vol. 106, no. 23234103, 2015, Art. no. 234103.

[38] L. Cheng and G. Y. Tian, "Transient thermal behavior of eddy-current pulsed thermography for nondestructive evaluation of composites," *IEEE Trans. Instrum. Meas.*, vol. 62, no. 5, pp. 1215–1222, May 2013.

[39] L. Cheng, B. Gao, G. Y. Tian, and W. L. Woo, "Impact damage detection and identification using eddy current pulsed thermography through integration of PCA and ICA," *IEEE Sensors J.*, vol. 14, no. 5, pp. 1655–1663, May 2014.

[40] R. Yang and Y. He, "Polymer-matrix composites carbon fibre characterisation and damage inspection using selectively heating thermography (SeHT) through electromagnetic induction," *Composite Struct.*, vol. 140, pp. 590–601, 2016.

[41] B. Gao, L. Bai, W. L. Woo, G. Y. Tian, and Y. Cheng, "Automatic defect identification of eddy current pulsed thermography using single channel blind source separation," *IEEE Trans. Instrum. Meas.*, vol. 63, no. 4, pp. 913–922, Apr. 2014.

[42] A. Yin, B. Gao, G. Y. Tian, W. L. Woo, and K. Li, "Physical interpretation and separation of eddy current pulsed thermography," *J. Appl. Phys.*, vol. 113, no. 6, 2013, Art. no. 064101.

[43] R. Yang and Y. He, "Optically and non-optically excited thermography for composites: A review," *Infrared Phys. Technol.*, vol. 75, pp. 26–50, 2016.

[44] Y. He, M. Pan, D. Chen, G. Tian, and H. Zhang, "Eddy current step heating thermography for quantitatively evaluation," *Appl. Phys. Lett.*, vol. 103, no. 19, 2013, Art. no. 194101.

[45] Y. He, M. Pan, and F. Luo, "Defect characterisation based on heat diffusion using induction thermography testing," *Rev. Sci. Instrum.*, vol. 83, no. 10104702, 2012, Art. no. 104702.

[46] Y. He *et al.*, "Eddy current pulsed phase thermography for subsurface defect quantitatively evaluation," *Appl. Phys. Lett.*, vol. 103, no. 14144108, 2013, Art. no. 144108.

[47] J. Wilson, G. Y. Tian, I. Z. Abidin, S. Yang, and D. Almond, "Pulsed eddy current thermography: System development and evaluation," *Insight*, vol. 52, no. 2, pp. 87–90, 2010.

[48] S.-C. Huang and B.-H. Chen, "Automatic moving object extraction through a real-world variable-bandwidth network for traffic monitoring systems," *IEEE Trans. Ind. Electron.*, vol. 61, no. 4, pp. 2099–2112, Apr. 2014.

[49] W. Ren *et al.*, "Quantitative non-destructive evaluation method for impact damage using eddy current pulsed thermography," *Composite Part B, Eng.*, vol. 54, no. 0, pp. 169–179, 2013.

[50] T. G. Kolda and B. W. Bader, "Tensor decompositions and applications," *SIAM Rev.*, vol. 51, no. 3, pp. 455–500, 2009.

[51] G. Y. Tian, A. Yin, B. Gao, J. Zhang, and B. Shaw, "Eddy current pulsed thermography for fatigue evaluation of gear," in *Proc. Amer. Inst. Phys. Conf.*, Baltimore, MD, USA, 2014, pp. 1652–1662.

[52] M. Vaidhianathasamy, B. A. Shaw, W. Bennett, and P. Hopkins, "Assessment of grinding damage on gear teeth using magnetic Barkhausen noise measurements," in *Proc. 12th Int. Workshop Electromag. Nondestruct. Eval.*, 2008, pp. 90–97.

[53] M. Vaidhianathasamy, B. A. Shaw, W. Bennett, and P. Hopkins, "Evaluation of contact fatigue damage on gears using the magnetic barkhausen noise technique," *Proc. 12th Int. Workshop Electromag. Nondestruct. Eval.*, 2008, pp. 98–105.

[54] V. Moorthy, B. A. Shaw, and P. Hopkins, "Magnetic Barkhausen emission technique for detecting the overstressing during bending fatigue in case-carburised En36 steel," *NDT&E Int.*, vol. 38, no. 2, pp. 159–166, 2005.

[55] M. R. Govindaraju, A. Strom, D. C. Jiles, S. B. Biner, and Z. J. Chen, "Evaluation of fatigue damage in steel structural components by magnetoelastic Barkhausen signal analysis," *J. Appl. Phys.*, vol. 73, no. 10, pp. 6165–6167, 1993.

[56] R. Yang and Y. He, "Logarithmic analysis of eddy current thermography based on longitudinal heat conduction for subsurface defect evaluation," *Infrared Phys. Technol.*, vol. 67, pp. 467–472, 2014.

[57] R. Yang, Y. He, B. Gao, G. Y. Tian, and J. Peng, "Lateral heat conduction based eddy current thermography for detection of parallel cracks and rail tread oblique cracks," *Measurement*, vol. 66, pp. 54–61, 2015.

Bin Gao (M'12–SM'14) received the B.Sc. degree in communications and signal processing from Southwest Jiao Tong University, Leshan, China, in 2005, and the M.Sc. degree in communications and signal processing with distinction and the Ph.D. degree in statistical signal processing from Newcastle University, Newcastle upon Tyne, U.K., in 2007 and 2011, respectively.

From 2011 to 2013, he was a Research Associate with Newcastle University, working on wearable acoustic sensor technology. He is currently an Associate Professor in the School of Automation Engineering, University of Electronic Science and Technology of China, Chengdu, China. His research interests include sensor signal processing, machine learning, social signal processing and nondestructive testing and evaluation, where he actively publishes in these areas. Dr. Gao is very active Reviewer for many international journals and long-standing conferences. He has coordinated several research projects from National Natural Science Foundation of China.

Yunze He (M'11) received the B.Sc. degree in measurement and control technology and instruments from Xi'an Jiaotong University, Xi'an, China, in 2006, and the M.Sc. and Ph.D. degrees in instrumentation science and technology from the College of Mechatronics Engineering and Automation, National University of Defense Technology, Changsha, China, in 2008 and 2012, respectively. He finished the joint Ph.D. degree at the School of Electrical, Electronic Engineering, Newcastle University, Newcastle upon Tyne, U.K., and the National University of Defense Technology, in February 2012.

He is currently an Associate Professor with the College of Electrical and Information Engineering, Hunan University, Changsha. His research interests include nondestructive testing and structural health monitoring. He has chaired or participated in more than 20 projects including those of the National Natural Science Foundation of China, Engineering and Physical Sciences Research Council, etc. He has published more than 50 academic papers in journals and conference proceeding, which have been cited more than 850 times. He has published three books. He is a Reviewer for more than 25 academic journals.

Wai Lok Woo (M'08–SM'11) received the B.Eng. degree (1st Class Hons.) in electrical and electronics engineering and the Ph.D. degree in higher order statistical signal processing from Newcastle University, Newcastle upon Tyne, U.K.

He received the IEE Prize and the British Scholarship to continue his research work. He is currently a Reader in Intelligent Signal Processing at Newcastle University. His major research interests include mathematical theory and algorithms for nonlinear signal and image processing. This includes the areas of machine learning for signal processing, blind source separation, multidimensional signal processing, signal/image deconvolution, and restoration. He has published more than 250 papers in various journals and conference proceedings. He currently serves on the Editorial Boards of several international signal processing journals. He actively organizes international conferences and workshops, and serves on their technical committees. He is a Consultant to a number of industrial companies that involve the use of statistical signal and image processing techniques.

Dr. Woo is a Member of the Institution of Engineering and Technology, U.K.

Gui Yun Tian (M'01–SM'03) received the B.Sc. degree in metrology and instrumentation and the M.Sc. degree in precision engineering from the University of Sichuan, Chengdu, China, in 1985 and 1988, respectively, and the Ph.D. degree in computing and engineering from the University of Derby, Derby, U.K., in 1998.

From 2000 to 2006, he was, successively, a Lecturer, Senior Lecturer, Reader, Professor, and the Head of the Group of Systems Engineering at the University of Huddersfield, U.K. Since 2007, he has been the Chair Professor in Sensor Technologies, Newcastle University, Newcastle upon Tyne, U.K. He is currently an Adjunct Professor with the School of Automation Engineering, University of Electronic Science and Technology of China, Chengdu, China. He has coordinated several research projects from the Engineering and Physical Sciences Research Council, Royal Academy of Engineering, and FP7. He also has good collaboration with leading industrial companies such as Airbus, Rolls Royce, BP, nPower, Networkrail, and TWI, among others.

Jia Liu received the B.Sc. degree from the School of Computer and Information Science, Southwest University, Chongqing, China, in 2008. She is currently working toward the M.Sc. degree in fatigue assessment and life cycle assessment using electromagnetic technique at the University of Electronic Science and Technology of China, Chengdu, China.

Her research interests include sensor signal processing, fatigue evaluating, structural health monitoring, and network security.

Yihua Hu (M'13–SM'15) received the B.S. degree in electrical motor drives and the Ph.D. degree in power electronics and drives from the China University of Mining and Technology, Jiangsu, China, in 2003 and 2011, respectively.

Between 2011 and 2013, he was a Postdoctoral Fellow with the College of Electrical Engineering, Zhejiang University. From November 2012 to February 2013, he was an Academic Visiting Scholar with the School of Electrical and Electronic Engineering, Newcastle University, Newcastle upon Tyne, U.K. Between 2013 and 2015, he worked as a Research Associate with the Power Electronics and Motor Drive Group, University of Strathclyde. He is currently a Lecturer in the Department of Electrical Engineering and Electronics, University of Liverpool, Liverpool, U.K. He has published more than 36 peer-reviewed technical papers in leading journals. His research interests include PV generation systems, power electronics converters and control, and electrical motor drives.